FULL PAPER

Open Access

2D resistivity model around the rupture area of the 2011 Tohoku-oki earthquake (*M*w 9.0)

Hiroshi Ichihara[1,2*] , Takafumi Kasaya[3], Kiyoshi Baba[4], Tada-nori Goto[5] and Makoto Yamano[4]

Abstract

The 2011 Tohoku-oki earthquake (*M*w 9.0) was characterized by a huge fault slip on the shallowest part of the plate interface, where fault behavior had been believed to be aseismic. In this study, we modeled the two-dimensional resistivity distribution across the slip area based on ocean-bottom electromagnetic measurements to understand the physical properties around the plate interface controlling fault rupture processes. The optimal 2D resistivity model showed a conductive area around the shallowest plate interface where the huge coseismic slip was observed, whereas the deeper plate interface where the fault rupture was nucleated was relatively more resistive. The shallowest plate interface was interpreted to have a high pore seawater fraction, whereas the deeper interface was interpreted as a dry area. These findings are consistent with the hypothesis that aseismic frictional conditions changed to conditions enhancing fault rupture when the rupture propagated to the wet, clay-rich shallowest plate area. The optimal resistivity model also revealed a conductive area under the outer-rise area of the Pacific Plate. This finding supports the existence of a hydrated oceanic crust that supplied aqueous water to the subduction zone, including to the huge fault slip area.

Keywords 2011 Tohoku-oki earthquake, Magnetotelluric, OBEM

Graphical Abstract
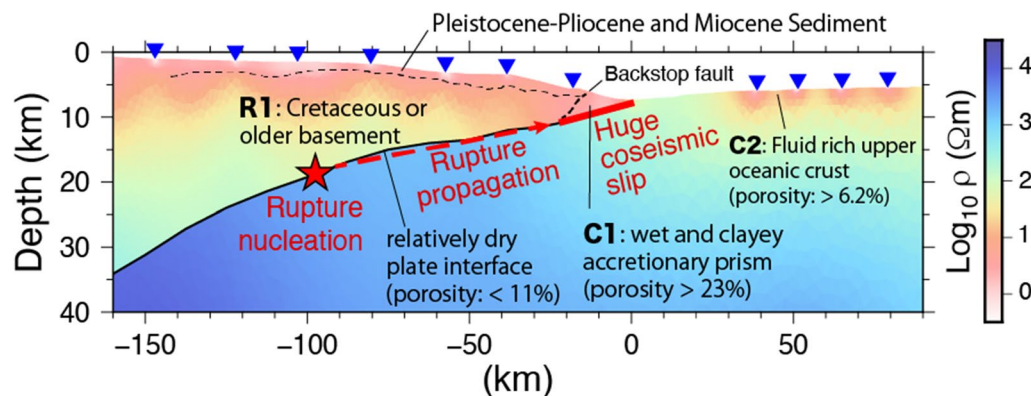
*Correspondence:
Hiroshi Ichihara
h-ichi@seis.nagoya-u.ac.jp
Full list of author information is available at the end of the article

Ichihara *et al. Earth, Planets and Space*   (2023) 75:82

Page 2 of 15

Introduction

The 2011 Tohoku-oki earthquake (M_w 9.0) was associated with a huge fault slip of more than 80 m in the shallowest part of the plate interface that possibly produced the devastating tsunami (e.g., Fujiwara et al. 2011; Ito et al. 2011; Iinuma et al. 2012) (Fig. 1). In the deeper part of the plate interface, the fault rupture nucleated but the estimated slip was smaller (e.g., Koketsu et al. 2011; Ide et al. 2011; Iinuma et al. 2012). The shallowest part of plate interface is usually aseismic because the consolidated sediments in this area enhance stable slip (e.g., Scholz 1998; Hyndman et al. 1997). Therefore, the huge shallow slip during the 2011 earthquake changed our understanding of megathrust earthquakes. Numerous studies have attempted to understand this fault slip behavior. The results of core sample experiments and borehole observations of the Japan Trench Fast Drilling Project (JFAST), carried out in the toe of the shallowest plate interface after the

earthquake (Fig. 1), suggest that when the fault rupture propagated with a high slip rate to the shallowest plate interface, the frictional properties changed to a state that enhanced fault slip because of the pelagic clay and high pore fluid pressure distributed there (e.g., Chester et al. 2013; Ujiie et al. 2013; Fulton et al. 2013). Thus, pore fluids made an essential contribution to the mega-slip mechanism.

Seismic and electromagnetic explorations have estimated that a highly hydrated zone exists in the crust and uppermost mantle of the oceanic plate just before it is subducted in some subduction zones, including in the Tohoku-oki area (e.g., Fujie et al. 2018; Naif et al. 2015). Because dehydration fluid from the subducted oceanic plate is a main source of aqueous fluid in a subduction zone, including in megathrust areas, it is important to investigate the amount of pore water in the incoming plate. Bending-related normal faulting in the outer-rise area, where the oceanic plate is bowed upward just before
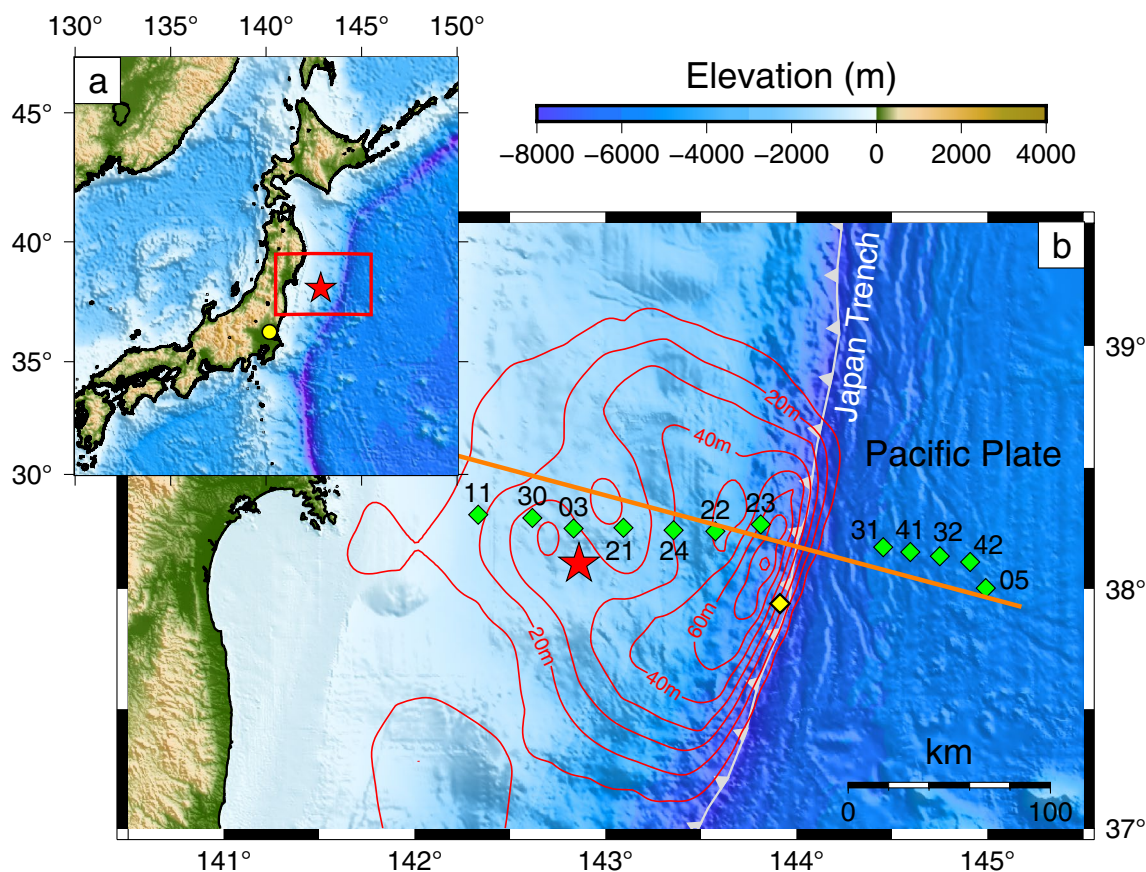
Fig. 1 Maps showing the study area location. The red star indicates the epicenter of the 2011 Tohoku-oki earthquake (M_w 9.0). Elevation data are from the ETOPO1 global relief model (NOAA 2009). **a** The open red rectangle indicates the area shown in **b**, and the yellow circle shows the location of the Kakioka Geomagnetic Observatory. **b** Green diamonds denote OBEM stations. The 2D models were constructed along the thick orange line. The yellow diamond indicates the JFAST borehole site (Chester et al. 2013). The red contours (10 m interval) show the fault slip during the 2011 Tohoku-oki earthquake based on (Iinuma et al. 2012)

Ichihara *et al. Earth, Planets and Space*   (2023) 75:82

Page 3 of 15

subduction, is believed to enhance hydration in the oceanic crust and uppermost mantle (e.g., Fujie et al. 2018). Moreover, because outer-rise faulting has caused devastating tsunamis (e.g., the 1933 off-Sanriku earthquake; Kanamori, (1972)), it is essential to understand the physical properties of the incoming plate.

Imaging of the electrical resistivity distribution gives insights into pore fluid and clay mineral distributions because the bulk resistivity greatly depends on the resistivity, amount, and connectivity of pore fluid and clay minerals. A magnetotelluric (MT) investigation uses electromagnetic signals from natural sources to image the resistivity distribution in the crust and upper mantle. For example, MT investigations have identified conductive zones along tectonic boundaries (e.g., Ichihara et al. 2016; Ikeda et al. 2013), suggesting that fluid-filled areas in and around fault zones may contribute to slip behavior at those boundaries. In the Tohoku-oki area, Key and Constable, (2011) analyzed marine MT data acquired from the forearc region (survey line along 40°N). They showed that the MT impedance data could constrain the thickness of surface conductive sediments and the underlying resistive zone associated with the mantle wedge and oceanic lithosphere despite strong coast effect distortions. Baba et al. (2017) estimated 1D resistivity profiles in the western Pacific plate (their "area D") and showed that a more than 100-km-thick resistive lithospheric layer overlies a conductive asthenospheric layer. However, the resistivity distribution near the focal zone of the 2011 Tohoku-oki earthquake has not been investigated. In this study, we used MT data acquired by ocean-bottom electromagnetic surveys to estimate the resistivity distribution around the focal area of the 2011 Tohoku-oki earthquake.

Data acquisition

We collected time series of electromagnetic data obtained by ocean-bottom electromagnetometers (OBEMs) deployed at 12 sites along a survey line crossing the center of the slip area of the 2011 Tohoku-oki earthquake and extending to the outer-rise area of the Pacific plate (Fig. 1). The OBEM investigations were carried out between 2009 and 2017 during 10 research cruises conducted by the Japan Agency for Marine-Earth Science and Technology (JAMSTEC) and the University of Tokyo (Additional file 1: Table S1). The OBEMs were deployed by being released from the ship and allowed to sink onto the seafloor. After data acquisition, the OBEMs released weights, surfaced, and were retrieved by the ship. Two types of OBEM were used for the measurements. A type developed by the University of Tokyo was deployed at sites 03 and 05. The other type, a small OBEM developed by JAMSTEC (Kasaya and Goto 2009), was deployed at

the other sites. Both types of OBEM measured two horizontal components of the electric potential difference with Ag–AgCl electrodes and three orthogonal components of the magnetic field with fluxgate magnetometers in a similar data quality. Time series of the electromagnetic signals, together with instrumental tilts and temperatures, were recorded at sampling intervals of 0.125, 10, or 60 s. The data were acquired over a period of 10 to 147 days, depending on the observation site. Magnetic fields were not available at site 42 because of an instrumental problem.

Magnetotelluric responses

We used frequency-domain MT impedance tensors ($\mathbf{Z}$) to image the resistivity distribution. $\mathbf{Z}$ is estimated from the two horizontal components of the electric field (E_x and E_y) and the magnetic field (B_x and B_y) as follows:

$$\begin{bmatrix} E_x \\ E_y \end{bmatrix} = \begin{bmatrix} Z_{xx} & Z_{xy} \\ Z_{yx} & Z_{yy} \end{bmatrix} \begin{bmatrix} B_x \\ B_y \end{bmatrix},$$

where subscripts x and y indicate geographic north and east, respectively. We also used geomagnetic transfer functions (GTFs) ($\mathbf{T}$), which reflect the horizontal gradient of the resistivity distribution, defined as follows:

$$B_z = \begin{bmatrix} T_x & T_y \end{bmatrix} \begin{bmatrix} B_x \\ B_y \end{bmatrix}.$$

We estimated $\mathbf{Z}$ and $\mathbf{T}$ from the recorded electric field and magnetic field time series using BIRRP code (Chave and Thomson 2004). The MT impedance at sites 31, 32, 41 and 42 were not well determined because of a low signal-to-noise ratio, especially in the short-period band (< 500 s); therefore, at these sites we applied FDICA-MT code (Sato et al. 2021) to estimate MT impedance based on the following reason. In deep seafloor where these sites locate, the electromagnetic signals and external-origin noises are decayed especially in the short periods and the signal power is comparable to the instrumental noise level. FDICA-MT can effectively decompose such data with low signal-to-noise ratio into MT signal and noise components, based on independent component analysis. In the estimations of MT impedances and GTFs, we applied the remote reference technique (Gamble et al. 1979) using horizontal magnetic field data from Kakioka Geomagnetic Station (Kakioka Magnetic Observatory 2013), which is more than 250 km southwest of the OBEM sites (Fig. 1). To estimate the impedance at site 42, we used geomagnetic field data at site 41 because magnetic field data for site 42 were not available. The estimated period range are between 171 and 524288 s for site 03 and 05; and are between 10.7 and 32768 s for the other sites. As a result, high-quality MT responses and

Ichihara *et al. Earth, Planets and Space* (2023) 75:82

Page 4 of 15

geomagnetic transfer functions were obtained at all sites except site 05 (Fig. 2).

We then used the MT impedances to evaluate the dimensionality and strike azimuth of the resistivity structure. Impedance values of the diagonal components of a 1D resistivity structure are zero ($Z_{xx} = Z_{yy} = 0$), and those of off-diagonal components are equivalent ($Z_{xy} = -Z_{yx}$). Impedance values of the diagonal components of a 2D resistivity structure are zero ($Z_{xx} = Z_{yy} = 0$) when the axes (x or y) are parallel or perpendicular to the strike azimuth. Therefore, on a polar diagram, the impedance amplitude of the diagonal components is zero for any coordinate azimuth of a 1D resistivity structure and for strike azimuth or its perpendicular azimuth of a 2D resistivity structure. On the other hands, off-diagonal components are unity on a polar diagram of a 1D resistivity structure and are typically maximized or minimized along the strike azimuth of a 2D resistivity structure.

While local resistivity anomalies near the MT station cause galvanic distortion that affects the polar diagram for land-based data, this issue is likely to be minimal in seafloor MT impedance due to the near-uniform conductivity of sediment beneath the seafloor (e.g., Key and Constable 2011). The polar diagrams are thus valuable tool for determining the dimensionality and the strike azimuth of the seafloor MT data. The polar diagrams for the 12 sites show that the amplitudes of the off-diagonal component impedance are maximized mostly in the 015–195° range for periods between 21 and 4096 s, except at site 05 (Additional file 1: Fig. S1), which are consistent with the strike direction of the subduction interface and bathymetry (010 to 190°–015 to 195°). The amplitudes of the diagonal components are much smaller than those of the off-diagonal components for these periods. These results indicate that the estimated MT impedance mostly reflects a 2D resistivity distribution. The phase tensors, which preserve the regional phase information regardless of the galvanic effects (Caldwell et al. 2004), also indicate a consistent geoelectrical azimuth with that of subduction interface and bathymetry (Additional file 1: Fig. S2).

GTF (**T**) is zero with a 1D resistivity distribution, whereas with a 2D resistivity structure, T_x is zero when the x-axis is defined by the strike azimuth. Considering this feature, we also used a GTF, graphically represented by Parkinson's induction vectors [Real{$-T_x$}, Real{$-T_y$}], [Imag{$-T_x$}, Imag{$-T_y$}] (Parkinson 1962), to examine the dimensionality of the resistivity structure. In a 2D resistivity distribution, direction of induction vector is perpendicular to the strike azimuth. The induction vector amplitudes in the study area are small for short-period MT data (≤ 256 s) and large for longer period data (Additional file 1: Figs. S1, S2). The vectors are dominantly directed toward 105° or 285° for periods between 256

and 4096 s, that is, approximately perpendicular to the contours of bathymetry and subduction interface. These features also indicate a 2D resistivity distribution with a strike azimuth of 015–195°.

Figure 2 shows sounding curves of the MT impedance, and GTFs, which were rotated to align with the strike azimuth of 015°. Low apparent resistivities and low phase values of short-period data imply a shallow, low-resistivity layer overlying a zone of higher resistivity. Cusps of apparent resistivity and impedance phases that are out of the ordinary quadrant are seen in the Z_{xy} component at a period of around 2000 s. These features have also been observed at 40°N in the Tohoku-oki area, where they were explained as a coast effect distortion due to the conductive seafloor at the OBEM site and to resistive earth beneath and adjacent to the OBEM (Key and Constable 2011). Extremely large GTF amplitudes are also seen at around 2000 s.

2D resistivity modeling

We used the 2D inversion code MARE2DEM (Key 2016) to construct resistivity models. MARE2DEM adopts arbitrarily shaped polygons for the inverse model and thus can efficiently replicate the complicated bathymetry and geometry of the plate interface. The inversion procedure minimizes the following objective function (*U*):

$$U = \|\mathbf{Rm}\|^2 + \mu^{-1}\|\mathbf{W}(\mathbf{d} - \mathbf{F}[\mathbf{m}])\|^2,$$

where **m** and **d** are the model parameter and the data parameter vector, respectively, and **R** is the model roughness operator. The first term on the right-hand side is a model roughness term, defined as the L_2 norm of the model gradient; this term, which is introduced to stabilize the inversion, is called the smoothness constraint. The second term is the data misfit term. **F**[**m**] is the vector of the forward response to **m**; **W** is a weight factor, defined as the inverse of the standard deviation of the data; and μ is a hyperparameter that balances the data misfit and model roughness terms. Note that we omitted the prejudice term shown in the original equation of Key (2016) (second term of Eq. 17). The inversion procedure uses the fast Occam's inversion approach to solve for **m** iteratively by varying μ (Constable et al. 1987).

For the modeling, we used the MT impedances and GTFs at periods between 42.7 and 4096 s rotated to align with the strike azimuth where x-axis is 015°, which indicated a 2D resistivity distribution as described in Sect. "Magnetotelluric responses". We omitted data that indicate 3D resistivity structure: (1) Swift's skewness (Swift 1967), a rotational invariant of MT impedance indicating asymmetry of the resistivity distribution, larger than 0.2 (Reddy et al. 1977), and (2) x-component of the induction vector with an absolute value greater
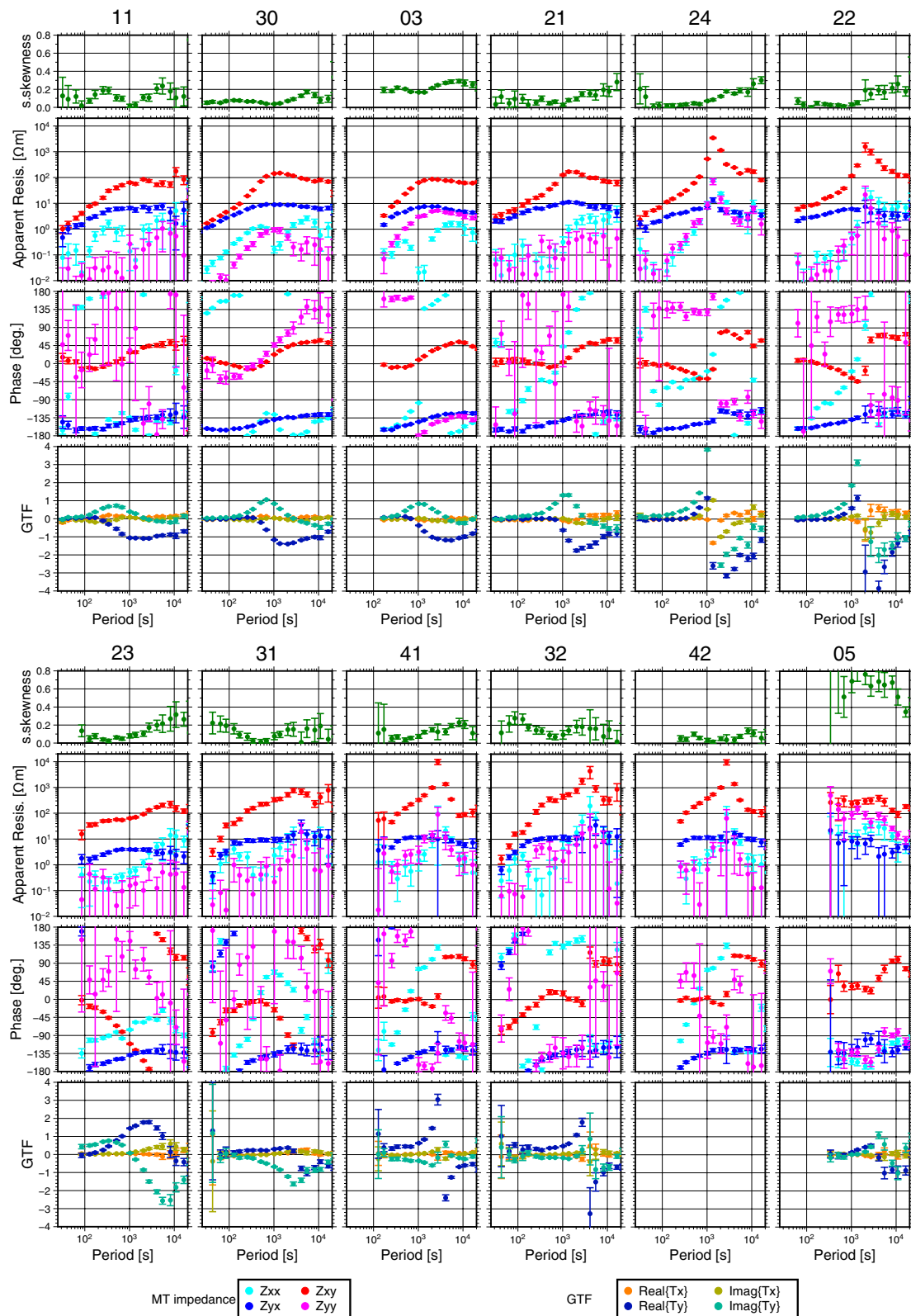
Ichihara *et al. Earth, Planets and Space*   (2023) 75:82

Page 5 of 15

Fig. 2 Sounding curves of Swift's skewness, apparent resistivity, and phase of the MT impedance, and the GTFs. The *x*- and *y*- axes are set at 015° and 105°, respectively

than 0.15 ($|T_x| > 0.15$) in either real or imaginary component. We selected the $|T_x|$ criterion but not $|T_x|/|T_y|$ because large $|T_x|/|T_y|$ values can occur in cases of small lateral heterogeneity when both $|T_x|$ and $|T_y|$ are small. We tested three values (0.05, 0.10 or 0.15) as the criterion of $|T_x|$ and chose 0.15 to avoid losing the data with large $|T_y|$ and small $|T_x|/|T_y|$ representing two-dimensional structures. We also excluded data at certain periods for specific sites: data at site 30 for periods of 128, 171 and 256 s due to a polar diagram showing a significant deviation from the assumed strike azimuth of 015°, and data at site 31 for periods of 85.3 and 128 s due to a large amplitude in the diagonal component of the MT impedance.

In total, 538 data parameters (Additional file 1: Fig. S1) were used in the inversions. An impedance amplitude of 10% and a GTF of 0.15 were applied as error floors. Error floors for marine MT impedance vary among studies (e.g., Tada et al. 2014 used 2.5% for off-diagonal components in a 3D inversion, while Chesley et al. 2021 used 10% for 2D inversion). As our study is based on a 2D assumption but the data could be affected by three-dimensional structure, we adopted a conservative error floor value to avoid overfitting to the data. We utilized data in which the *x*-component of the induction vector was less than 0.15. This implies that 0.15 can serve as the minimum error of the GTF and is consequently utilized as the error floor. We set 3.0 as the horizontal-to-vertical penalty weight (w_{hv}) in the roughness term to inhibit unrealistic horizontal variations (Key 2016).

Three-layered model
The out-of-quadrant phases and cusps of apparent resistivity in the Z_{xy} component make the inversion problem difficult (e.g., Worzewski et al. 2012). To avoid model trapping into local minima in the inversion procedure, the initial model should explain such data. Key and Constable (2011) approximated such MT responses observed along 40°N by a simple 2D model consisting of three homogeneous resistivity layers: seawater, a subseafloor conductive layer reflecting seafloor sediment, and the underlying background. Therefore, we first estimated the initial inversion model to be a simplified three-layered resistivity model. The resistivity of the seawater layer was fixed at 0.3 Ωm during the inversion procedures. The bathymetry was based on the ETOPO-1 model (NOAA 2009). We divided the subseafloor layer into areas landward and seaward of the Japan Trench. The thickness of the landward subseafloor layer was set to 1.5 km because seismic reflection surveys have shown the sediment thickness in the Tohoku-oki area to be between 1 and 2 km (Kodaira et al. 2017). Similarly, the thickness of the seaward subseafloor layer was set to 0.3 km because seismic reflection surveys have shown sediment thickness to

be between 0.2 and 0.4 km near the OBEM survey line (Fujie et al. 2020). In total, three parameters (the resistivities of the two subseafloor layers and the background) were solved using the MARE2DEM code, but the model roughness term was omitted because the number of data (538) was much larger than the number of model parameters (3).

As the result of the preliminary inversion, we obtained resistivities of 0.93, 0.23, and 277 Ωm for the landward subseafloor layer, the seaward subseafloor layer, and the background, respectively (Model 0, Fig. 3). Model-predicted responses predominantly explain the observed data, including the out-of-quadrant phases, the cusp of apparent resistivity in the Z_{xy} component, and the anomalously large GTF (root mean square (RMS) misfit: 2.582) (Fig. 4, Additional file 1: Figs. S1, S2). However, the resistivity model needs to be improved because the responses do not adequately fit to data such as the apparent resistivity split between the Z_{xy} and Z_{yx} components at the seaward sites.

Inverted resistivity models
We next estimated 2D resistivity distributions using Model 0 as the initial model. The same data set as was used for the three-layered modeling (subsect. "Three-layered model") was used for the inversions described below.

Resistivity boundaries may be distributed along the bottom of the subseafloor conductive layer because the resistivity of the seafloor sediment (1–2 Ωm in the JFAST borehole; Chester et al. 2013; Fig. 1) is considerably smaller than that of crustal materials (e.g., chert, basalt, gabbro, and consolidated sedimentary rock). In addition, because the plate interface is a lithological boundary, it may also be a resistivity boundary. In fact, Kodaira et al. (2017) have reported a marked velocity contrast on the plate interface near the trench. Therefore, we conducted inversion procedures using the following four settings:

- Model smoothness is equally applied in the whole region (Model I).
- Model smoothness is reduced along the bottom of the subseafloor layer to 10% of the smoothness of other regions (Model II).
- Model smoothness is reduced along the plate interface to 10% of the smoothness of other regions (Model III).
- Model smoothness is reduced along both the bottom of the subseafloor layer and the plate interface to 10% of the smoothness of other regions (Model IV).

In Models III and IV, the location of the western part of plate interface ($y < -50$ km) is based on PS converted
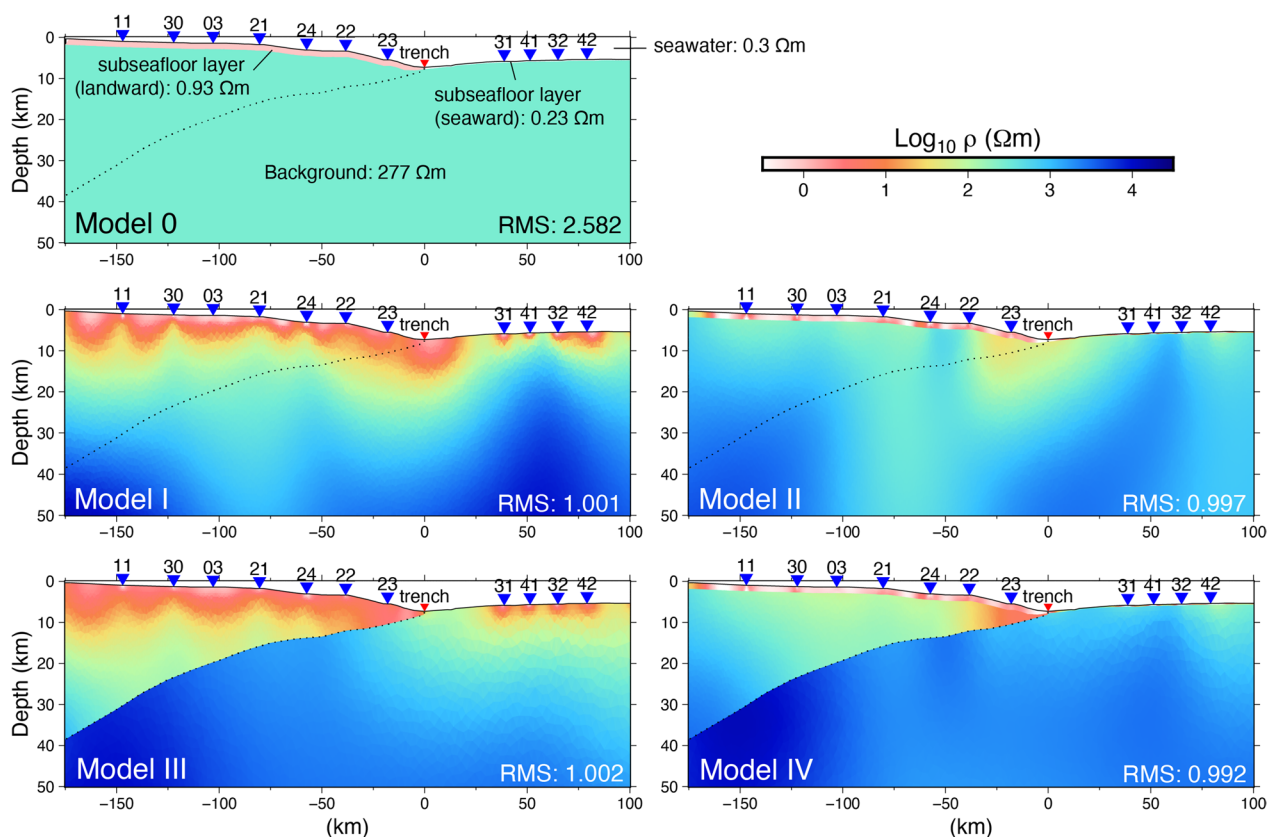
Fig. 3 Model 0 (initial model) and the inverted resistivity profiles of Models I–IV. Blue inverse triangles denote the OBEM stations. The horizontal and vertical scale ratio of images is 1:2

seismic waves (Zhao et al. 1997) (Fig. 3). In the eastern part (− 50 km < *y* < 0 km), we set the boundary based on the reflection plane and the V_p distribution estimated by seismic surveys (Kodaira et al. 2017).

The inverted models were obtained after the 7–10 iterations of the inversion procedure. All of the models explained most of the data (Fig. 4, Additional file 1: Figs. S4–S7); the RMS misfits were reduced to 1.001, 0.997, 1.002, and 0.992 for Models I, II, III, and IV, respectively. Thus, all the inversions mostly reached the target RMS misfit value (1.000). The inverted resistivity models roughly showed a three-layered resistivity distribution: (1) a conductive subseafloor layer (from the seafloor to < 10 km depth; < 10 Ωm); (2) a resistive layer (40–150 km deep; 1000–20,000 Ωm); and 3) an underlying conductive layer (< 10 Ωm) (Fig. 3, Additional file 1: S8). These features are basically consistent with the resistivity distribution in and under the Pacific plate estimated about 1000 km offshore from the study area (Baba et al. 2013, 2017) and hence indicate that the rough structure in and under the Pacific plate is maintained around the Japan trench.

Validity of the resistivity model
All of the models showed an obvious conductive area around the eastern edge of the upper plate (area **C1** in Fig. 5) although the distribution of the conductive area varied among the models. These results indicate the robustness of **C1** independent of the smoothness constraint. The differences among the models are due to poor resolution in the shallow area as well as to the differences in the smoothness constraint. Indeed, model-predicted MT impedances at periods shorter than the periods of the inverted data were significantly different among the models (Additional file 1: Figs. S4–S7). The results also imply that the shorter period data are important for the resistivity distribution in the shallow area.

The resistivity of the subseafloor layer in Models I and III (0.5–4 Ωm near the OBEM stations) is consistent with the resistivity of seafloor sediments (typically 1–2 Ωm, e.g., Chester et al. 2013). In Models II and IV, however, some areas are unrealistically conductive, especially near the OBEM stations (< 0.3 Ωm). The unrealistic conductive areas can be attributed to the reduced smoothness beneath the sediment layer. Therefore, Models I and III
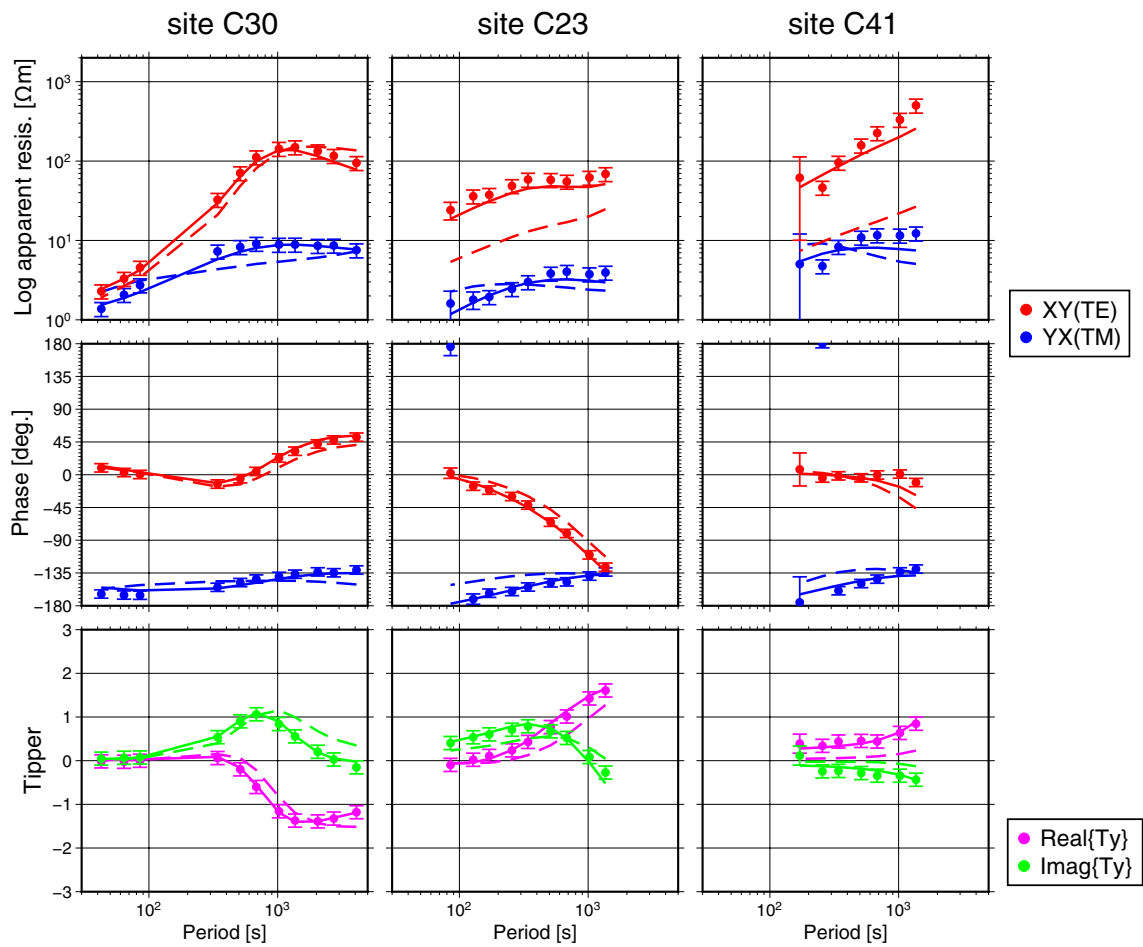
Fig. 4 Sounding curves at sites 30, 23, and 41. Dots with error bars show observed data. Error bars include the error floor (see text). The dashed and solid lines are the responses predicted by the initial model used for the inversion (Model 0) and the optimal model (Model III), respectively
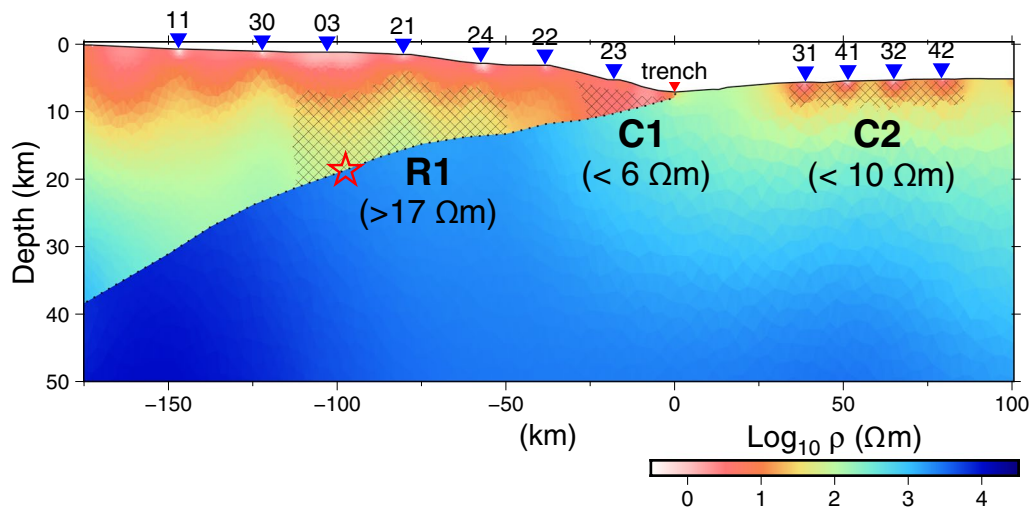

Fig. 5 Resistivity Model III showing the areas used for validation. The **C1**, **C2,** and **R1** areas are hashed. The open red star denotes the hypocenter of the 2011 Tohoku-oki earthquake. The horizontal and vertical scale ratio of images is 1:2

Ichihara *et al. Earth, Planets and Space*   (2023) 75:82

Page 9 of 15

seem more compatible with the real resistivity distribution than Models II and IV.

Borehole logging at the JFAST site showed a sudden resistivity increase with depth around the plate interface caused by the geological change from pelagic clay to chert (Chester et al. 2013). Moreover, a clear seismic reflective plane associated with a change of V_P near the plate interface (Nakamura et al. 2014) suggests that the geological change is extended along the plate interface. These findings imply the existence of a resistivity gap along the plate interface. Therefore, we adopted Model III as the optimal model in this study.

We evaluated the sensitivity of conductive area **C1** on the landward side of the Japan Trench (2–6 Ωm in Model III), which includes the area of huge coseismic slip of over 80 m during the 2011 Tohoku-oki earthquake (e.g., Iinuma et al. 2012). In our evaluation, we modified the optimum model to obscure the **C1** anomaly and then calculated the model responses. In the modified models, the lower limits of resistivity were values between 3 and 7 Ωm between 1 km depth of the seafloor and the plate interface, between $y=0$ km (trench axis) and -27 km (Fig. 5). In other words, we replaced areas where the resistivity was less than 3–7 Ωm with resistivities of 3–7 Ωm. A one-sided *F*-test showed at the 95% confidence level that the variance of the normalized residuals between the observed and calculated responses of the modified models was significantly larger than that of the inverted model when the lower limit was larger than 6 Ωm (Fig. 6). Therefore, resistivity in **C1** should be less than 6 Ωm.

Next, we examined the deep resistive area **R1** in the upper plate ($y=-110$ to -50 km, Fig. 5), which includes the hypocenter (where the fault rupture initiated) of the 2011 earthquake. We modified the upper limit of the resistivity in that area to a value between 12 and 50 Ωm (Fig. 5) and calculated the model responses. A one-sided *F*-test showed at the 95% confidence level that the variance of the residuals of the modified models with an upper limit smaller than 17 Ωm was significantly large compared to the optimum model (Fig. 6). These test results indicate that the resistivity of the upper plate (excluding the surface conductive layer) is significantly larger in the deeper **R1** area than that in the shallow **C1** area.

The optimum model shows a conductive zone beneath the sediment layer on the seaward side of the trench (area **C2** in Fig. 5). Area **C2** is not an artifact caused by the deep extension of the conductive subseafloor layer (to 300 m depth below the seafloor) by the smoothness constraint because the resistivity values of 0.6–2.0 Ωm just beneath the seafloor in the optimum model are consistent with those of seafloor sediments in the Tohoku-oki area (Chester et al. 2013) and an additional conductive area is required to explain the low apparent resistivities and high phases of the MT impedances at sites 31, 41, 32, and 42 (Fig. 2 and Additional file 1: Fig. S6). In addition, the resistivity is too low (0.2–0.7 Ωm) in the seafloor sediment in Models II and IV, in which the smoothness constraint was reduced beneath the sediment layer. This indicates that the subseafloor conductive sediment layer does not adequately explain the low apparent resistivities and high phases of the MT impedances at sites 31, 41, 32, and 42 (Additional file 1: Figs. S5 and S7).

To constrain the resistivity of area **C2**, we modified the lower resistivity limit in the area from the bottom of the subseafloor layer to a depth of about 9 km to 4–15 Ωm (Fig. 5) and calculated the model responses. A one-sided
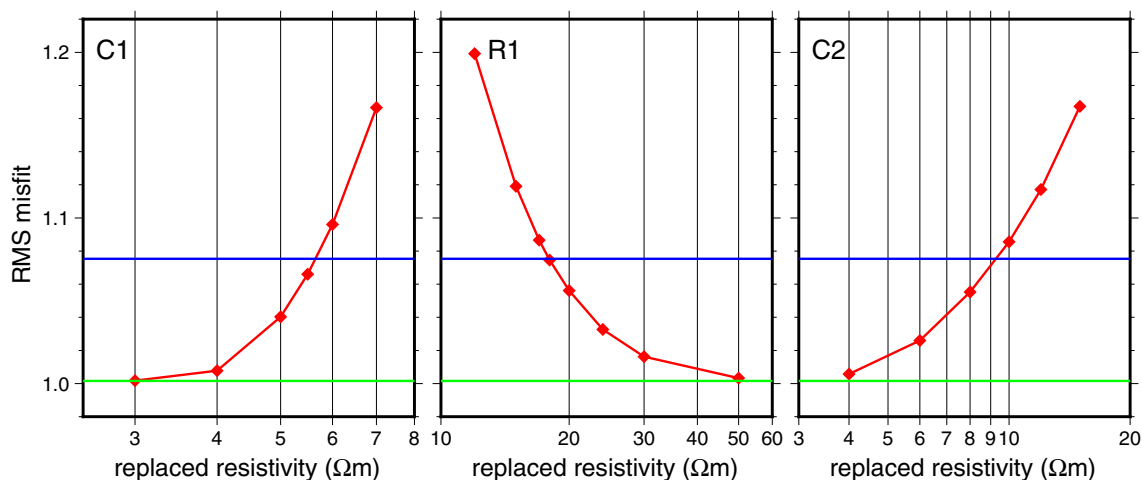

Fig. 6 RMS misfit of sensitivity test models for the conductive areas **C1** and **C2**, and the resistive area **R1**. The green and blue lines denote the RMS misfit of the inverted model (Model III) and the 95% confidence limit of the *F*-test, respectively

F-test showed at the 95% confidence level that the variance of the residuals of the models in which the upper limit of resistivity was replaced with a value of less than 10 Ωm was significantly large compared with that of the optimal model (Fig. 6).

Discussion

Pore fluid distribution and geological interpretations

Saline pore fluid is the main factor controlling resistivity beneath the seafloor around the subduction margin (e.g., Naif et al. 2016). Therefore, we evaluated porosity based on Archie's law (Archie, 1942), an empirical relationship between resistivity and porosity:

$$\rho_0 = \rho_w \phi^{-m},$$

where ρ_0 is rock bulk resistivity, ρ_w is resistivity of the pore fluid, ϕ is porosity, and m is a cementation exponent. Thus, the pore fluid volume fraction ($=\phi$) can be obtained from ρ_0 when ρ_w and m are known. Using this relationship, we estimated the pore fluid contents in conductive areas **C1** and **C2** and the resistive area **R1**, where the sensitivity tests constrained the bulk resistivity (ρ_0) range. In these calculations, ρ_w was derived by using a function relating it to temperature (T) and the

NaCl concentration (c) based on formulas determined experimentally by Bannard (1975) and Sakuma and Ichiki (2016). We assumed the NaCl concentration c to be 3.4 wt%, which is equivalent to the general seawater salt concentration and consistent with that in pore waters in the JFAST borehole, which was drilled in the **C1** area (Expedition 343/343T Scientists 2013)

Conductive frontal prism zone (C1)

Geological and seismic studies have indicated that unconsolidated sediments have accreted on the upper plate between the trench axis and the backstop fault in the area called the accretionary or frontal prism (Fig. 7) (e.g., von Huene et al. 1994; Chester et al. 2013; Kodaira et al. 2017; Tsuru et al. 2000). The eastern part of low-resistivity zone **C1**, constrained by the sensitivity test to have a resistivity (ρ_0) of less than 6 Ωm, corresponds to the frontal prism area.

To evaluate ϕ in the shallow (eastern) and deep (western) parts of the plate interface at the frontal prism, we estimated ρ_w and m. Temperature (T) is 27.3 °C at the depth of the fault slip area in the JFAST borehole, which is located at the eastern edge of the frontal prism (Fig. 1) (Fulton et al. 2013), and temperature in the deepest part
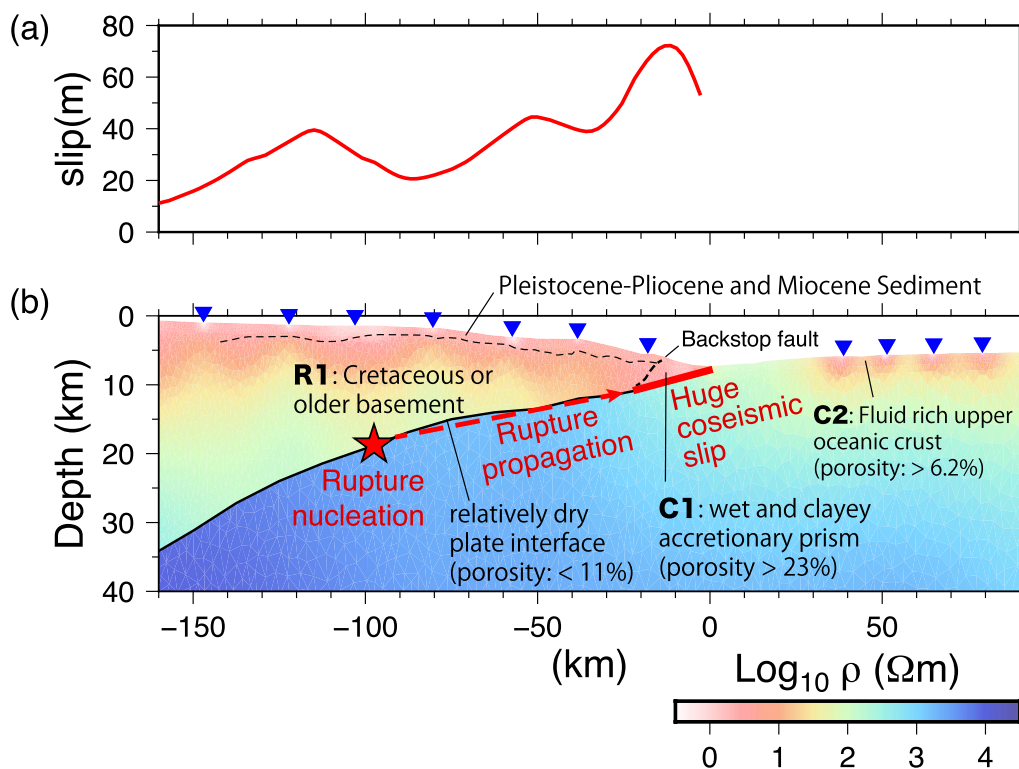

Fig. 7 **a** Coseismic slip distribution below the OBEM survey line during the 2011 Tohoku-oki earthquake (Iinuma et al. 2012). **b** The optimal resistivity model (Model III) with interpretation. Thick and thin dashed lines denote the backstop fault and the bottom of the subseafloor sediment layer based on a seismic survey at line TH03 (Kodaira et al. 2017), respectively. The horizontal and vertical scale ratio of images is 1:2

of the frontal prism is less than 100 °C, based on Hyndman and Peacock (2003). Using these temperatures, we calculated ρ_w to be between 0.177 and 0.070 Ωm on the plate interface at the eastern and western end, respectively, of the frontal prism. For m in the frontal prism, we adopted the value of 3.0, which we obtained by minimizing the RMS misfit between the measured and calculated porosities based on data from the JFAST borehole (Expedition 343/343T Scientists 2013) and temperature (Fulton et al. 2013) (for details see Additional file 1: Document and Table S2). Then, using these parameters, we calculated porosity in the plate interface area to be 30.7% at the eastern end and 22.7% at the western end of the frontal prism. Note that these estimated porosities are a lower limit because the bulk resistivity (ρ_0) of 6 Ωm estimated by the sensitivity test is an upper limit. The estimated porosities correspond to the measured porosity (35–53%) around the plate interface in the JFAST borehole as well as to estimates based on seismic velocity (Hondori and Park 2022). Therefore, our result implies that the pore fluid content is high in the frontal prism. A high V_p/V_S anomaly (>1.8) estimated by seismic tomography also supports a high fluid fraction in the **C1** area (Yamamoto et al. 2014).

Area **C1** also extends to the west of the backstop fault (outside of the frontal prism), where Cretaceous or older basement rocks are distributed, but the data resolution is too low to examine precise resistivity values within **C1**. Kodaira et al. (2017) estimated that ∼2% of the sediment on the oceanic plate is accreted to the frontal prism and the other ∼98% is subducted at the plate interface. Thus, to the west of the backstop fault, **C1** may reflect subducting sediment or dehydration fluid derived from the subducting sediments by compaction, which occurs a few tens of kilometers from the trench axis (Hyndman and Peacock 2003) (Fig. 7). Additional OBEM observations between the existing observation sites are needed to confirm this hypothesis.

Resistive upper plate (R1)
To the west of the backstop fault, Cretaceous or older sedimentary rocks (basement rock) underlie the subseafloor sediment layers that formed from the Miocene to the Pleistocene (von Huene et al. 1994; Kodaira et al. 2017). The upper part of pre-Tertiary rocks and the newer sediment layers correspond spatially to the subseafloor conductive layer whereas the lower part of pre-Tertiary rocks correspond to **R1** (Fig. 7). The depth variation of resistivity within the pre-Tertiary rocks should attribute to porosity variation. Here, we estimated the porosity at the bottom of **R1** (plate interface) by using Archie's law and assuming the following parameters. The sensitivity test constrained the resistivity to be more than 18 Ωm

in **R1**. ρ_w was calculated to be 0.070 Ωm when the temperature (T) was set at 100 °C, based on a contour map of thermal structure at $y=-75$ km (Hyndman and Peacock 2003). We assumed the standard range of m for sedimentary rocks (1.5–2.5; Gueguen and Palciauskas, 1994), because there is no constraint for m available from this area. Using these parameters, we estimated porosity to be from 2.6% ($m=1.5$) to 11.1% ($m=2.5$) in the upper plate along the plate boundary. Note that the actual porosities are lower than the estimates because the resistivity of 18 Ωm is a lower limit. Therefore, a significant reduction of the pore fluid content along the plate interface from the **C1** area to the **R1** area is validated. The low-to-moderate V_p/V_S also supports a relatively low fluid fraction in the **R1** area (Yamamoto et al. 2014).

Conductive oceanic crust in the incoming plate (C2)
The low-resistivity area **C2** (<10 Ωm) underlies the conductive sediment layer in the seaward of the trench area. Because this zone is within oceanic crustal material consisting of basalt and gabbro, which has high resistivity under dry, low-temperature conditions, pore fluid is again the likely candidate to explain the decreased resistivity. Using Archie's law, we estimated porosity to be more than 6.2% (18.9%) when m was assumed to be 1.5 (2.5). In this calculation, we also assumed the temperature to be 30 °C based on the average temperature profile beneath the sediment layer in the outer-rise Tohoku-oki area (Kawada et al. 2014). The porosity value (>6.2%) suggests a higher amount of pore fluid than that typically found in normal oceanic crust, as the porosity of sheeted dike and gabbro in oceanic crusts were estimated to be 3.0% and 0.7%, respectively (Jarrard 2003). This result thus supports the inference of hydration of the oceanic crust in the outer-rise area indicated by the seismic velocity distribution (e.g., Fujie et al. 2018, 2016).

Hydration in bending faults is thought to be a cause of high water content in outer-rise areas (e.g., Fujie et al. 2018). However, the sparse OBEM observation sites and the lack of short-period MT responses due to signal attenuation in the deep sea prevented us from imaging the resistivity distribution in the outer-rise area in detail. By integrated analyses of natural source MT and controlled electromagnetic investigations, Naif et al. (2016) showed with high resolution the resistivity distribution around the Mid-American Trench that indicates saline pore fluid along the bending faults. Therefore, investigation utilizing dense OBEM deployments and controlled-source electromagnetic surveys are essential to reveal the distribution of the saline pore fluid. In this study, OBEMs could not be deployed around the Japan Trench (between sites 23 and 31) because the water depth there (>6000 m) means that the water pressure exceeds the

Ichihara *et al. Earth, Planets and Space* (2023) 75:82

Page 12 of 15

operating limits of the present instruments. This trench area is also important because the pore fluid in **C2** would be a source of aqueous fluid to the subduction zone and the pore water content should increase toward the trench (e.g., Fujie et al. 2018). Hence, investigations with OBEMs designed for ultra-deep-sea deployment are essential for investigating water transport in the subduction zone.

Implications for megathrust earthquakes

The shallowest parts of plate interfaces are generally considered to be aseismic, and, in fact, earthquakes have rarely nucleated around the frontal prism in the Tohoku-oki area (Obana et al. 2013; Yamamoto et al. 2014). This aseismicity can be explained by velocity-strengthening frictional behavior (where friction increases with slip rate) (e.g., Scholz 2019), and the clay-rich sediments in this area are compatible with this behavior. The fault rupture during the 2011 Tohoku-oki earthquake caused >80 m of displacement in this area (e.g., Ide et al. 2011; Iinuma et al. 2012). This large slip can be explained by a change of the frictional behavior from velocity-strengthening to velocity-weakening when the slip rate became high and the clay became saturated with pore water (e.g., Faulkner et al. 2011). In the case of the 2011 earthquake, a very low friction coefficient and velocity-weakening behavior were demonstrated around the earthquake fault in the JFAST borehole by high-slip-rate friction experiments on core samples (Ujiie et al. 2013) and temperature measurements (Fulton et al. 2013). Our results support the existence of a high amount of pore fluid in the frontal prism (Fig. 7), which would enhance the velocity-weakening behavior. In addition, seismic data analyses have indicated that a fault rupture was propagated from the deeper rupture zone with high slip rate (e.g., Ide et al. 2011). Therefore, conditions in the frontal prism were appropriate for the occurrence of a huge coseismic slip when the fault rupture propagated from the deeper plate interface.

The 2011 Tohoku-oki earthquake fault rupture was initiated in the **R1** area (Koketsu et al. 2011; Ide et al. 2011) (Fig. 7). This area has been considered to be a major rupture (stick–slip) area (Yamanaka and Kikuchi 2004), and the largest foreshock of the 2011 earthquake (*M*w 7.3) also originated there (e.g., Gusman et al. 2012). Therefore, **R1** is an area where the frictional conditions caused stick–slip behavior. The relatively dry conditions of **R1** are compatible with such behavior because a high pore fluid pressure decreases the strength of the interface.

This study clarified the resistivity structure at the plate boundary, including the frontal prism near the Japan Trench axis, based on natural source MT data, and thereby constrained the pore fluid amount that controlled the 2011 Tohoku-oki earthquake. Although the very deep and steep bathymetry around the Japan Trench made the analyses challenging, we expect to be able to elucidate the resistivity structure more easily in other subduction zones, which have mostly shallower and less resistivity contrast. Additionally, it is expected that the structure of the entire subduction zone will be elucidated by joint analysis of marine and land MT data in the future. The resistivity structure is sensitive to fluid distribution and is independent of the velocity structure obtained using seismic waves. Hence, a comprehensive interpretation of both structures, with increased precision, can significantly enhance our comprehension of subduction zones, including megathrust earthquakes. However, while there have been multiple studies focusing on plate boundary earthquakes using seismic waves, only a limited number of research on resistivity structures have been conducted. Consequently, it is crucial to conduct future research to determine the resistivity structure with high accuracy.

Conclusions

Marine magnetotelluric investigations were conducted at 12 sites across the rupture zone of the Tohoku-oki earthquake (*M*w 9.0). The MT impedances and GTFs obtained from the electromagnetic data show a strong coast effect, which complicated modeling of the resistivity structure. Thus, we first constructed a simple three-layered 2D resistivity model consisting of seawater, subseafloor conductive sediment layers, and the underlying background materials. This model reasonably explained the observed data, including the coast effect. Then, we estimated the 2D resistivity distributions in more detail by conducting inversion procedures using the three-layered model as the initial model. We proposed four models with different roughness conditions along the base of the subseafloor conductive layer and along the plate interface. After consideration of the actual resistivity distribution, we adopted the model that showed a resistivity gap along the plate interface but not along the base of the subseafloor conductive layer as the optimal resistivity model (Model III). According to the optimal model, the upper plate is conductive (**C1**, <6 Ωm) at its eastern edge, whereas the western part of the plate interface is resistive (**R1**, >17 Ωm). The eastern part of **C1** was interpreted to be an accretionary (frontal) prism containing a large amount of pore water (>22.7%). The deeper resistive part was interpreted as a relatively dry area composed of Cretaceous or older basement rocks (<11.1%). These structural conditions are compatible with the fault slip behavior observed during the Tohoku-oki earthquake; the fault rupture was nucleated on the deep dry plate interface and then propagated to the shallow wet, clayey part of the plate interface with a high slip rate, which changed the frictional

Ichihara *et al. Earth, Planets and Space*   (2023) 75:82

Page 13 of 15

behavior there to velocity-weakening and resulted in a huge coseismic slip. In addition, a low-resistivity zone (**C2**, < 10 Ωm) estimated in the upper crust of the Pacific oceanic plate implies hydration of the oceanic crust in the incoming Pacific plate.

Abbreviations
MT   Magnetotelluric
GTF   Geomagnetic transfer function

Supplementary Information
The online version contains supplementary material available at https://doi.org/10.1186/s40623-023-01828-1.

Additional file 1: Table S1. Summary of the ocean-bottom electro-magnetometer observations. **Figure S1.** Polar diagrams showing the relative magnitudes of Z_{xx} and Z_{xy}. **Figure S2.** Phase tensor ellipses and Parkinson's induction vectors. **Figure S3.** Sounding curves of observed and model-predicted impedances of Model 0. **Figure S4.** Sounding curves of observed and model-predicted impedances of Model I. **Figure S5.** Sounding curves of observed and model predicted impedances of Model II. **Figure S6.** Sounding curves of observed and model-predicted impedances of Model III. **Figure S7.** Sounding curves of observed and model-predicted impedances of Model IV. **Figure S8.** Inverted resistivity profiles. **Additional Document.** Estimation of cementation exponent (*m*) in the frontal prism area. **Table S2.** Physical parameters of borehole C0019.

Author contributions
All of the authors contributed to the observations. HI and KB analyzed the data. All authors contributed to the interpretation of the data and approved the final manuscript. All authors read and approved the final manuscript.

Availability of data and materials
Contact the corresponding author to access the digital data underpinning the 2D resistivity model.

Declarations

Ethics approval and consent to participate
Not applicable.

Consent for publication
Not applicable.

Competing interests
The authors declare that they have no competing interests regarding this study.

Author details
[1]Earthquake and Volcano Research Center, Graduate School of Environmental Studies, Nagoya University, Furo-cho, Chikusa-ku, Nagoya 464-8601, Japan. [2]Research Institute for Marine Geodynamics, Japan Agency for Marine-Earth Science and Technology, 2-15 Natsushima-cho, Yokosuka 237-0061, Japan. [3]Research Institute for Marine Resources Utilization, Japan Agency for Marine-Earth Science and Technology, 2-15 Natsushima-cho, Yokosuka 237-0061, Japan. [4]Earthquake Research Institute, The University of Tokyo, 1-1-1 Yayoi, Bunkyo-Ku, Tokyo 113-0032, Japan. [5]Graduate School of Science, University of Hyogo, 2167 Shosha, Himeji 671-2280, Japan.

References
Archie GE (1942) The electrical resistivity log as an aid in determining some reservoir characteristics. Trans AIME 146:54–62

Baba K, Tada N, Zhang LL, Liang PF, Shimizu H, Utada H (2013) Is the electrical conductivity of the northwestern Pacific upper mantle normal? Geochem Geophys Geosyst 14(12):4969–4979. https://doi.org/10.1002/2013gc004997

Baba K, Tada N, Matsuno T, Liang PF, Li RB, Zhang LL, Shimizu H, Abe N, Hirano N, Ichiki M, Utada H (2017) Electrical conductivity of old oceanic mantle in the northwestern Pacific I: 1-D profiles suggesting differences in thermal structure not predictable from a plate cooling model. Earth Planets Space. https://doi.org/10.1186/s40623-017-0697-0

Bannard JE (1975) Effect of density on the electrical conductance of aqueous sodium chloride solutions. J Appl Electrochem 5:43–53

Caldwell TG, Bibby HM, Brown C (2004) The magnetotelluric phase tensor. Geophys J Int 158(2):457–469

Chave AD, Thomson DJ (2004) Bounded influence magnetotelluric response function estimation. Geophys J Int 157(3):988–1006. https://doi.org/10.1111/J.1365-246x.2004.02203.X

Chesley C, Naif S, Key K, Bassett D (2021) Fluid-rich subducting topography generates anomalous forearc porosity. Nature. https://doi.org/10.1038/s41586-021-03619-8

Chester FM, Rowe C, Ujiie K, Kirkpatrick J, Regalla C, Remitti F, Moore JC, Toy V, Wolfson-Schwehr M, Bose S, Kameda J, Mori JJ, Brodsky EE, Eguchi N, Toczko S, Scientist E, Scientist ET (2013) Structure and Composition of the plate-boundary slip zone for the 2011 Tohoku-Oki earthquake. Science 342(6163):1208–1211. https://doi.org/10.1126/Science.1243719

Constable SC, Parker RL, Constable CG (1987) Occams inversion— a practical algorithm for generating smooth models from electromagnetic sounding data. Geophysics 52(3):289–300

Expedition 343/343T Scientists (2013) Proceedings of the Integrated Ocean Drilling Program (Vol. 343/343T). http://publications.iodp.org/proceedings/343_343T/103/103_.htm. Accessed 30 Nov 2022

Faulkner DR, Mitchell TM, Behnsen J, Hirose T, Shimamoto T (2011) Stuck in the mud? Earthquake nucleation and propagation through accretionary forearcs. Geophys Res Lett. https://doi.org/10.1029/2011gl048552

Fujie G, Kodaira S, Sato T, Takahashi T (2016) Along-trench variations in the seismic structure of the incoming Pacific plate at the outer rise of the northern Japan Trench. Geophys Res Lett 43(2):666–673. https://doi.org/10.1002/2015gl067363

Fujie G, Kodaira S, Kaiho Y, Yamamoto Y, Takahashi T, Miura S, Yamada T (2018) Controlling factor of incoming plate hydration at the north-western Pacific margin. Nat Commun. https://doi.org/10.1038/s41467-018-06320-z

Fujie G, Kodaira S, Nakamura Y, Morgan JP, Dannowski A, Thorwart M, Greve-meyer I, Miura S (2020) Spatial variations of incoming sediments at the northeastern Japan arc and their implications for megathrust earthquakes. Geology 48(6):614–619. https://doi.org/10.1130/G46757.1

Fujiwara T, Kodaira S, No T, Kaiho Y, Takahashi N, Kaneda Y (2011) The 2011 Tohoku-Oki earthquake: displacement reaching the trench axis. Science 334(6060):1240–1240. https://doi.org/10.1126/Science.1211554

Fulton PM, Brodsky EE, Kano Y, Mori J, Chester F, Ishikawa T, Harris RN, Lin W, Eguchi N, Toczko S, Scientist E, Scientist ET, Scientist EK (2013) Low coseismic friction on the tohoku-oki fault determined from temperature measurements. Science 342(6163):1214–1217. https://doi.org/10.1126/Science.1243641

Gamble TD, Clarke J, Goubau WM (1979) Magnetotellurics with a remote magnetic reference. Geophysics 44(1):53–68

Gueguen Y, Palciauskas V (1994) Introduction to the physics of rocks. Princeton University Press, Princeton

Gusman AR, Tanioka Y, Sakai S, Tsushima H (2012) Source model of the great 2011 Tohoku earthquake estimated from tsunami waveforms and crustal deformation data. Earth Planet Sci Lett 341–344:234–242

Hondori EJ, Park JO (2022) Connection between high pore-fluid pressure and frictional instability at tsunamigenic plate boundary fault of 2011 Tohoku-Oki earthquake. Sci Rep. https://doi.org/10.1038/s41598-022-16578-5

Hyndman RD, Peacock SM (2003) Serpentinization of the forearc mantle. Earth Planet Sci Lett 212(3–4):417–432. https://doi.org/10.1016/S0012-821x(03)00263-2

Hyndman RD, Yamano M, Oleskevich DA (1997) The seismogenic zone of subduction thrust faults. Isl Arc 6(3):244–260. https://doi.org/10.1111/J.1440-1738.1997.Tb00175.X

Ichihara H, Mogi T, Tanimoto K, Yamaya Y, Hashimoto T, Uyeshima M, Ogawa Y (2016) Crustal structure and fluid distribution beneath the southern part of the Hidaka collision zone revealed by 3-D electrical resistivity modeling. Geochem Geophys Geosyst 17(4):1480–1491. https://doi.org/10.1002/2015gc006222

Ide S, Baltay A, Beroza GC (2011) Shallow dynamic overshoot and energetic deep rupture in the 2011 M(w) 9.0 Tohoku-oki earthquake. Science 332(6036):1426–1429. https://doi.org/10.1126/science.1207020

Iinuma T, Hino R, Kido M, Inazu D, Osada Y, Ito Y, Ohzono M, Tsushima H, Suzuki S, Fujimoto H, Miura S (2012) Coseismic slip distribution of the 2011 off the Pacific Coast of Tohoku Earthquake (M9.0) refined by means of seafloor geodetic data. J Geophys Res Sol Earth. https://doi.org/10.1029/2012jb009186

Ikeda M, Kato S, Nishizaka N, Ohno Y, Matsuo K, Kishimoto M (2013) Magnetotelluric imaging of the Median Tectonic Line in western Shikoku, southwest Japan: implications of the fault-related low-resistivity zone. Tectonophysics 601:78–86. https://doi.org/10.1016/j.tecto.2013.04.026

Ito Y, Tsuji T, Osada Y, Kido M, Inazu D, Hayashi Y, Tsushima H, Hino R, Fujimoto H (2011) Frontal wedge deformation near the source region of the 2011 Tohoku-Oki earthquake. Geophys Res Lett. https://doi.org/10.1029/2011gl048355

Jarrard RD (2003) Subduction fluxes of water, carbon dioxide, chlorine, and potassium. Geochem Geophys Geosyst. https://doi.org/10.1029/2002gc000392

Kakioka Magnetic Observatory (2013) Kakioka geomagnetic field 1-second digital data in IAGA-2002 format. Kakioka Magnetic Observatory Digital Data Service. https://doi.org/10.48682/186bd.58000

Kanamori H (1972) Mechanism of tsunami earthquake. Phys Earth Planet Inter 6:346–359

Kasaya T, Goto T (2009) A small ocean bottom electromagnetometer and ocean bottom electrometer system with an arm-folding mechanism. Explor Geophys 40(1):41–48. https://doi.org/10.1071/Eg08118

Kawada Y, Yamano M, Seama N (2014) Hydrothermal heat mining in an incoming oceanic plate due to aquifer thickening: explaining the high heat flow anomaly observed around the Japan Trench. Geochem Geophys Geosyst 15(4):1580–1599. https://doi.org/10.1002/2014gc005285

Key K (2016) MARE2DEM: a 2-D inversion code for controlled-source electromagnetic and magnetotelluric data. Geophys J Int 207(1):571–588. https://doi.org/10.1093/gji/ggw290

Key K, Constable S (2011) Coast effect distortion of marine magnetotelluric data: insights from a pilot study offshore northeastern Japan. Phys Earth Planet Inter 184(3–4):194–207. https://doi.org/10.1016/j.pepi.2010.11.008

Kodaira S, Nakamura Y, Yamamoto Y, Obana K, Fujie G, No T, Kaiho Y, Sato T, Miura S (2017) Depth-varying structural characters in the rupture zone of the 2011 Tohoku-oki earthquake. Geosphere 13(5):1408–1424. https://doi.org/10.1130/Ges01489.1

Koketsu K, Yokota Y, Nishimura N, Yagi Y, Miyazaki S, Satake K, Fujii Y, Miyake H, Sakai S, Yamanaka Y, Okada T (2011) A unified source model for the 2011 Tohoku earthquake. Earth Planet Sci Lett 310(3–4):480–487. https://doi.org/10.1016/J.Epsl.2011.09.009

Naif S, Key K, Constable S, Evans RL (2015) Water-rich bending faults at the Middle America Trench. Geochem Geophys Geosyst 16(8):2582–2597. https://doi.org/10.1002/2015gc005927

Naif S, Key K, Constable S, Evans RL (2016) Porosity and fluid budget of a water-rich megathrust revealed with electromagnetic data at the Middle America Trench. Geochem Geophys Geosyst 17(11):4495–4516. https://doi.org/10.1002/2016gc006556

Nakamura Y, Kodaira S, Cook BJ, Jeppson T, Kasaya T, Yamamoto Y, Hashimoto Y, Yamaguchi M, Obana K, Fujie G (2014) Seismic imaging and velocity structure around the JFAST drill site in the Japan Trench: low Vp, high Vp/Vs in the transparent frontal prism. Earth Planet Space. https://doi.org/10.1186/1880-5981-66-121

NOAA NGDC (2009) ETOPO1 1 Arc-minute global relief model. https://doi.org/10.7289/V5C8276M

Obana K, Kodaira S, Shinohara M, Hino R, Uehira K, Shiobara H, Nakahigashi K, Yamada T, Sugioka H, Ito A, Nakamura Y, Miura S, No T, Takahashi N (2013) Aftershocks near the updip end of the 2011 Tohoku-Oki earthquake. Earth Planet Sci Lett 382:111–116. https://doi.org/10.1016/j.epsl.2013.09.007

Parkinson WD (1962) The influence of continents and oceans on geomagnetic variations. Geophys J R Astron Soc 6(4):441–449

Reddy IK, Rankin D, Phillips RJ (1977) Three-dimensional modelling in magnetotelluric and magnetic variational sounding. Geophys J Int 51(2):313–325. https://doi.org/10.1093/gji/51.2.313

Sakuma H, Ichiki M (2016) Electrical conductivity of NaCl-H2O fluid in the crust. J Geophys Res Sol Earth 121(2):577–594. https://doi.org/10.1002/2015jb012219

Sato S, Goto TN, Kasaya T, Ichihara H (2021) Method for obtaining response functions from noisy magnetotelluric data using frequency-domain independent component analysis. Geophysics 86(1):E21–E35. https://doi.org/10.1190/Geo2018-0792.1

Scholz CH (1998) Earthquakes and friction laws. Nature 391(6662):37–42. https://doi.org/10.1038/34097

Scholz CH (2019) The mechanics of earthquakes and faulting, 3rd edn. Cambridge University Press, Cambridge. https://doi.org/10.1017/9781316681473

Swift CMA (1967) Magnetotelluric Investigation of an Electrical Conductivity Anomaly in the Southwestern United States. Ph. D thesis, Massachusetts Institute of Technology, MA, USA

Tada N, Baba K, Utada H (2014) Three-dimensional inversion of seafloor magnetotelluric data collected in the Philippine Sea and the western margin of the northwest Pacific Ocean. Geochem Geophys Geosyst 15(7):2895–2917. https://doi.org/10.1002/2014gc005421

Tsuru T, Park JO, Takahashi N, Kodaira S, Kido Y, Kaneda Y, Kono Y (2000) Tectonic features of the Japan Trench convergent margin off Sanriku, northeastern Japan, revealed by multichannel seismic reflection data. J Geophys Res Sol Earth 105(B7):16403–16413

Ujiie K, Tanaka H, Saito T, Tsutsumi A, Mori JJ, Kameda J, Brodsky EE, Chester FM, Eguchi N, Toczko S, Scientist E, Scientist ET (2013) Low coseismic shear stress on the Tohoku-oki megathrust determined from laboratory experiments. Science 342(6163):1211–1214. https://doi.org/10.1126/Science.1243485

von Huene R, Klaeschen D, Cropp B (1994) Tectonic structure across the accretionary and erosional parts of the Japan Trench margin. J Geophys Res Sol Earth 99(B11):22349–22361. https://doi.org/10.1029/94jb01198

Wessel P, Luis JF, Uieda L, Scharroo R, Wobbe F, Smith WHF, Tian D (2019) The generic mapping tools version 6. Geochem Geophys Geosyst 20(11):5556–5564. https://doi.org/10.1029/2019gc008515

Worzewski T, Jegen M, Swidinsky A (2012) Approximations for the 2-D coast effect on marine magnetotelluric data. Geophys J Int 189(1):357–368. https://doi.org/10.1111/J.1365-246x.2012.05385.X

Yamamoto Y, Obana K, Kodaira S, Hino R, Shinohara M (2014) Structural heterogeneities around the megathrust zone of the 2011 Tohoku earthquake from tomographic inversion of onshore and offshore seismic observations. J Geophys Res Sol Earth 119(2):1165–1180. https://doi.org/10.1002/2013jb010582

Yamanaka Y, Kikuchi M (2004) Asperity map along the subduction zone in northeastern Japan inferred from regional seismic data. J Geophys Res Sol Earth. https://doi.org/10.1029/2003jb002683

Zhao DP, Matsuzawa T, Hasegawa A (1997) Morphology of the subducting slab boundary in the northeastern Japan arc. Phys Earth Planet Inter 102(1–2):89–104. https://doi.org/10.1016/S0031-9201(96)03258-X

Publisher's Note

Springer Nature remains neutral with regard to jurisdictional claims in published maps and institutional affiliations.